Revision 1 Word count: 8802

Internal Stress-induced recrystallization and diffusive transport in $CaTiO_3$-$PbTiO_3$ solid solutions: A new transport mechanism in geomaterials and its implications for thermobarometry, geochronology and geospeedometry

Christopher Beyer[*1] and *Sumit Chakraborty*[1]

[1]Institut für Geologie, Mineralogie und Geophysik, Ruhr-Universität Bochum, Universitätsstr. 150, 44780 Bochum, Germany

*corresponding author, christopher.c.beyer@rub.de

Abstract

We conducted a series of high-temperature experiments where single crystals of $CaTiO_3$ were embedded in $PbTiO_3$ powder for durations of 4 to 502 hours at temperature between 753 and 1207 °C. Combined with results from a previous study (Beyer et al. 2019), these experiments allow us to explore the influence of chemical potential gradients on the mechanisms of incorporation of Pb in $CaTiO_3$. Unlike in the previous study where Pb diffused into $CaTiO_3$, here we find that the rims of the $CaTiO_3$ crystals recrystallize to form a polycrystalline aggregate of $(Pb_xCa_{(1-x)})TiO_3$ solid solutions. The width of the recrystallized front increases with run duration and the contact to the single crystal becomes progressively wavy. The concentration of Pb decreases within the recrystallized front toward the interior of the single crystal and the newly formed crystals are of different chemical compositions and orientation, and are themselves chemically zoned. There is a discontinuous jump in Pb-concentration at the contact of the

recrystallized front with the single crystal (termed *the migrating interface*). The development of chemical concentration gradients, combined with the fact that the width of the front grows as the square-root of time indicates a role of diffusion in the process; the formation of new crystals with different composition and no orientation relation to the precursor, and the jump in concentration at the boundary between the newly formed crystals and the single crystal indicates a dissolution-precipitation type process. Thus, this is a novel mechanism where diffusion as well as dissolution-precipitation (in the sense that the structure of the single crystal is destroyed and replaced by new crystals) occur simultaneously in a coupled manner and neither is rate-determining. The observations in this experimental study provide several insights into the mechanisms of chemical transformation in such non-metallic materials: (i) chemical differences can trigger mechanical deformation, which in turn can control chemical fluxes, (ii) newly formed crystals, even at the high temperatures of the experiments, evolve continuously in chemistry and are not of an equilibrium composition, (iii) the activation energy of the overall process (~ 70 kJ/mol) is lower than that for diffusion and provides a more effective means of chemical transformation, even though diffusion plays a central role in the process, and (iv) it underscores the role of surface / interface free energy in the evolution of the transformation process. These results have important consequences for the reading of the petrological and geochemical signatures of the rock record – notably, in addition to knowing when a phase becomes chemically stable, it is also important to know when a particular crystal of the phase begins to exist. Some possible implications for thermobarometry, isotopic dating and geospeedometry / diffusion chronometry are discussed.

Keywords: diffusion, recrystallization, lattice strain, kinetics, perovskite

45

46 ## Introduction

47 The understanding of geological processes and the evolution of rocks through space and time
48 relies on the chemical and isotopic signatures that are preserved during their formation and
49 equilibration with coexisting phases. Geothermobarometry (Ramberg and DeVore 1951; Urey et
50 al. 1951; Essene 1982) isotope geochronology (Patterson 1956; Wetherill 1956; Tera and
51 Wasserburg 1972) and geospeedometry (Dodson 1973; Lasaga 1983) are all tools that were
52 developed to make use of the fact that chemical transformations occur in mineralogical systems
53 in response to changes in intensive thermodynamic variables such as pressure, temperature or
54 chemical environment as a function of time. For application of these tools to natural systems, it is
55 also essential to know how compositions or structural features readjust themselves in response to
56 changes in intensive variables (for example, during heating or cooling, see Dodson 1973). Two
57 processes that are widely considered in this context are those of diffusion of chemical species and
58 dissolution / precipitation in response to chemical driving forces (Dodson 1973; Lasaga et al.
59 1977; Walther and Wood 1984). More recently, it has been demonstrated that coupled processes,
60 where for example, diffusion and dissolution-precipitation occur in parallel, provide perhaps a
61 more realistic description of natural processes (e.g. Jonas et al. 2015).

62 In this study, building on our previous work on diffusion of Pb in $CaTiO_3$ (Beyer et al. 2019)
63 we present results of experiments on $CaTiO_3$ that demonstrate how chemical potential gradients
64 can induce simultaneous recrystallization and diffusion. The system $CaTiO_3$ – $PbTiO_3$ forms a
65 complete solid solution series with a structural phase transition at 0.416 mol% $CaTiO_3$ (Chandra
66 and Pandey 2011). The mineral is of interest for dating and isotopic finger printing in e.g.
67 kimberlites and lamproites (i.e. Tappe and Simonetti 2012). What makes the solid solution series

especially intriguing for this study is the large difference between the sizes of Ca^{2+} and Pb^{2+}, the resulting difference in unit cell volumes (Δr = 0.15 Å , ΔV =11%), and the large Young's modulus (254 GPa). The combination of these properties makes the system particularly suitable for studying the effect of strain resulting from chemical change. We interpret the novel observations of this study to result from deformation due to internal stresses generated in the crystal lattice due to chemical change. We conclude by discussing some of the potential implications of this newly discovered phenomenon for geothermobarometry, isotope geochemistry and geochronology and geospeedometry.

Methods

We used natural perovskite single crystals from Zlathust, Russia, with a composition of > 99% $CaTiO_3$ (major and trace elements are given in Table 1). The crystals are opaque and were examined optically to check for cracks and larger impurities. We cut the pre-selected crystals, using a diamond wire saw, to rectangular prims with approximate dimensions of 1 x 1 x 3 mm, with the c-axis oriented parallel to the longest face. One side of the crystal, parallel to the c-axis, was polished with a succession of diamond pastes and alumina colloids. We cleaned the slices with acetone and distilled water in an ultrasonic bath and embedded them in finely ground synthetic $PbTiO_3$ powder within a platinum capsule (~ 4 x 6 mm outer dimensions). The capsules were welded shut on both sides using a PUK U5 arc welder. $PbTiO_3$ powder was prepared from analytical grade PbO (99.999 % purity) and TiO_2 (99.8 % purity) and blended in stoichiometric proportions with an excess of 5 wt.% PbO to compensate for Pb-loss through evaporation. The reagents were finely ground in an agate mortar and heated to 900 °C for at least 8 hours in air to

obtain $PbTiO_3$ with the tetragonal crystal structure *P4mm*, which was confirmed by powder X-ray diffraction (XRD) (Figure 1).

We conducted two different kinds of experiments: (a) a time series from 4 to 502 hours, heat-treated at 1118 °C, and (b) a temperature series from 753 °C to 1207 °C with run durations of 23 ½ hours each (Table 2). All experiments were carried out in a Nabertherm LHT02/17 high-temperature furnace. The temperature was monitored with an S-type thermocouple, which was placed close to the capsules. Temperatures were stable within 1 °C of the temperature set point that was controlled with a PID controller.

We checked the recovered capsules for fissures and potential Pb-loss. The reacted $CaTiO_3$ crystals were extracted from the capsule and cleaned in an ultrasonic bath to remove adhering $PbTiO_3$ powder. We embedded the crystals into epoxy resin and ground them parallel to the longest dimension. Subsequently, the cross-sections were polished with a succession of diamond paste (down to 0.25 µm particle size) and finished with alumina colloid (0.05 µm particle size) to produce a smooth and even surface for subsequent analyses. All samples were coated with a 10 nm thick layer of carbon before being examined with electron beam techniques.

The samples were analyzed using a Zeiss Gemini 2 field-emission scanning electron microscope (FE-SEM) at the Ruhr-Universität Bochum. We used back-scatter electron imaging (BSE) to evaluate compositional heterogeneities. The orientation of recrystallized grains and sub-grains was analyzed using electron backscatter diffraction (EBSD) on an area with the dimensions of ~ 50 by 75 µm (stepsize 0.458 µm) with a Nordlys EBSD detector. The sample was tilted to an angle of 70°. The data was evaluated with the software AztecICE from Oxford Instruments. The width of the newly grown crystal layers was quantified using composite back scattered electron images stacked with the open-source software FIJI (imageJ).

The concentration profiles, normal to the crystal surface, were analyzed with a Cameca SX-Five field emission electron microprobe analyzer (EMPA) at the Ruhr Universität Bochum. We used a beam current of 20 nA and an acceleration voltage of 15 kV. The following reference materials were employed: Wollastonite (Ca), apatite (P), $Pb_3Si_2O_7$ (Pb), and rutile (Ti). Peak counting times were 20 s, and background counting times were 10 s. The profile step width was set between 2 and 5 µm. Furthermore, we took high quality WDX (wavelength-dispersive X-rays) maps of major elements to investigate chemical gradients and possible zonations in the two-dimensional space. All data were processed using the X-PHI correction (Merlet 1994).

The trace element content of the natural perovskite crystals was determined by means of Laser ablation inductive coupled plasma mass spectrometry (LA ICP-MS) at the Institute of Mineralogy, University of Münster. The analytical setup consists of a 193 nm ArF excimer laser (Analyte G2 Photon Machines) attached to a Thermo Fisher Element XR mass spectrometer. Forward power was 1250 W and reflected power < 1 W, gas flow rates were 1.1 l/m for He (carrier gas of ablated material), 0.9 l/m and 1.1 l/m for the Ar-auxiliary and sample gas, respectively. Cooling gas flow rate was set to 16 l/min. Before starting analysis, the system has been tuned (torch position, lenses, gas flows) on a NIST 612 glass measuring ^{139}La, ^{232}Th and $^{232}Th^{16}O$ to get stable signals and high sensitivity, as well as low oxide rates ($^{232}Th^{16}O/^{232}Th$ < 0.1%) during ablation. The laser spot size on standards and samples was 85 µm using a repetition rate of 10 Hz.

NIST SRM 612 was used as the primary reference material and BHVO-2G and GSE-1D were employed for cross-checking the calibration. The Ca concentration measured with the EMPA was used as internal standard for the data reduction using the software GLITTER (Griffin 2008). The following isotopes were measured: ^{23}Na, ^{29}Si, ^{43}Ca, ^{45}Sc, ^{47}Ti, ^{49}Ti, ^{56}Fe, ^{85}Rb, ^{88}Sr, ^{89}Y, ^{90}Zr,

This is the peer-reviewed, final accepted version for American Mineralogist, published by the Mineralogical Society of America.
The published version is subject to change. Cite as Authors (Year) Title. American Mineralogist, in press.
DOI: https://doi.org/10.2138/am-2021-7588. http://www.minsocam.org/

136 ^{93}Nb, ^{133}Cs, ^{137}Ba, ^{139}La, ^{140}Ce, ^{141}Pr, ^{146}Nd, ^{147}Sm, ^{153}Eu, ^{157}Gd, ^{159}Tb, ^{163}Dy, ^{165}Ho, ^{166}Er, ^{169}Tm,
137 ^{172}Yb, ^{175}Lu, ^{178}Hf, ^{181}Ta, ^{195}Pt, ^{208}Pb, ^{232}Th, ^{238}U.

138 Although we took great care in sectioning normal to the crystal face, we cannot rule out
139 minor deviations from normal sectioning. Hence, we measured the width of two opposing rims
140 and calculated the average rim width. Assuming a tilt of 5° from normal, which is probably the
141 upper limit introduced by sample grinding and polishing, the corresponding uncertainty in profile
142 length is found to be less than 0.5 %, applying standard trigonometric functions. We avoided
143 rounded corners and areas with cracks to obtain comparable widths throughout the experimental
144 series.

145

146 **Results**

147 **Texture of run products**

148 In this study, all $CaTiO_3$ single crystals developed new polycrystalline rims of $(Ca,Pb)TiO_3$
149 solid solutions with varying thickness and structure that were functions of both, annealing time
150 and annealing temperature (Table 2, Figure 2). The newly-formed crystals partially replaced the
151 original single crystal and are not the result of crystal-overgrowth on the surface of the pre-
152 existing $CaTiO_3$ crystal. This can be seen from the measured sizes and shapes of the single crystal
153 – microcrystal aggregate. Moreover, the recrystallized rims are very dense with practically no
154 porosity or inclusions of $PbTiO_3$ powder, which also suggests that the crystallizing front
155 propagated into the $CaTiO_3$ crystal and not into the $PbTiO_3$ powder. It follows from this that a
156 reaction front migrated *into* the single crystal by replacing $CaTiO_3$ with a solid solution of
157 $(Pb_xCa_{(1-x)})TiO_3$, where x decreases towards the $CaTiO_3$ - $(Pb_xCa_{(1-x)})TiO_3$ interface. Intriguingly,

158 the new interface (called *migrating interface* in the following) between the $CaTiO_3$ single crystal
159 and the polycrystalline rim has an undulating and non-uniform shape comparable to the shapes of
160 interfaces observed in chemically induced grain boundary migration experiments with calcite
161 (Evans et al. 1986). On the other hand, the *original interface* (between the initial single crystal
162 and the $PbTiO_3$ source) retained the straight shape of the polished $CaTiO_3$ crystal. The
163 wavelength and amplitude of roughness of the *original interface* and the *migrating interface* are
164 clearly different – while the small variation from flatness in the former resulted from the
165 polishing stage of sample preparation, the much more enhanced variation in the latter resulted
166 from the chemical exchange process.

167 Internally, the rims are composed of intergrown micro-grains that themselves usually show a
168 distinct chemical gradient between core and the rim closer to the contact with the undisturbed
169 (but chemically modified, see below) single crystal (Figure 3). The micro-grains have a large
170 variety of shapes, ranging from polyhedra with ~ 120 ° triple junctions through elongated crystals
171 to subhedral rounded structures with a less distinct crystal habit (Figure 3). The size of the grains
172 varies between 4 and 30 µm and shows no correlation with the distance to the *migrated interface*.

173 Some $CaTiO_3$ crystals show cracks, likely caused by the thermal shock during the transfer of
174 the capsules out of the furnace. Fissures and cracks that already existed before the experiment are
175 filled by a thin layer of recrystallized $(Pb_xCa_{(1-x)})TiO_3$ solid solutions (Figure 2) whereas crystals
176 that cracked after the experiment are blank.

177 The inverse pole figures calculated form the EBSD analyses show that the crystals in the rim
178 are randomly oriented, and do not show any lattice-preferred orientation (Figure 4).

179

This is the peer-reviewed, final accepted version for American Mineralogist, published by the Mineralogical Society of America.
The published version is subject to change. Cite as Authors (Year) Title. American Mineralogist, in press.
DOI: https://doi.org/10.2138/am-2021-7588. http://www.minsocam.org/

180 **Apatite precipitation**

181 In some experiments, the *original interface* of the crystals is decorated by a thin non-
182 continuous layer of apatite crystals, whereas, in some other experiments, we observed needle-
183 shaped apatite crystals oriented normal to the crystallization front (Figure 5). We propose that the
184 natural perovskite released phosphorus (~ 0.5 wt% P_2O_5 was detected in the crystal bulk) during
185 the formation of new crystals and precipitated apatite. Comparison of the texture and profile
186 lengths from experiments with and without apatite crystals indicate that this precipitation process
187 did not affect the recrystallization process of the perovskite solid solution series that was the
188 object of this study.

189

190 **Chemical composition**

191 As noted above, the concentration of Pb decreases from the *original interface* to the
192 *migrating interface* [Region I]. At the *migrating interface*, there is a discontinuous drop in the
193 concentration of Pb to a lower value but not to zero [Region II]. From that point on, there is a
194 diffusive front / profile of Pb ahead of the *migrating interface* into the single crystal [Region III]
195 (Figure 5). Note that the presence of the third region is backed by observations of our previous
196 study (see Beyer et al. 2019), where we applied time-of-flight secondary ion mass spectrometry
197 (TOF-SIMS) and Rutherford backscattering spectrometry (RBS) to measured diffusion profiles
198 of Pb in $CaTiO_3$ single crystals (μg/g level concentrations).

199 The concentration of Pb in the $(Pb_xCa_{(1-x)})TiO_3$ solid solution of the micro-crystalline, newly
200 formed rim near the *original interface* is high but variable, ranging between 25 and 98 mol%
201 depending on the duration of the experiment (Figure 6). In other words, the concentration at the

original interface increases gradually with time and does not attain a composition equal to that of the source (100 mol% $PbTiO_3$) instantaneously.

In Region I, with increasing distance from the *original interface*, the Pb-component decreases until the solid solution contains only 13 to 26 mol% Pb. The final composition close to the *migrating interface* in Region II is similar for all experiments, with a mean composition of 15 mol% Pb and a standard deviation of 3 mol% Pb (Figure 7). The concentration of Pb at the migrating interface appears to decrease with increasing run durations (Figure 7). Beyond the migrating interface in Region III one observes a regular diffusion profile of Pb into the single crystal of $CaTiO_3$ (cf. Figure 2 in Beyer et al. (2019)).

Although the overall change of composition of the solid solution across Regions I-III defines a front that is sub-parallel to the *original interface*, the Pb-isopleths are undulated, indicating a distinct component of flux in a direction parallel to the interface. The form of these isopleths tracks the evolving shape of the *migrating interface* (Figure 3 and Figure 5) and is a function of time. Hence, local concentration gradients between the newly-formed crystals expand the observed process to a distinctly two-dimensional problem.

Pb-loss

In some experiments, TiO_2 was found in the powder source after the runs, indicating that some Pb must have been lost. However, this does not seem to have affected the width of the rims formed because the profile lengths and internal structures in the experiments where Pb-loss occurred (e.g. Pv_Pb_D4 and Pv_Pb_D5) are indistinguishable from experiments that retained their Pb completely. The only difference between these two kinds of experiments is in the

maximum concentration of $PbTiO_3$ at the *original interface*, with a lower concentration in experiments where Pb-loss occurred. This results in a profile with a flattened gradient. We assume that as long as the concentration in the source is high enough, recrystallization happens. Only if the concentration decreases significantly, i.e. <0.2 Pb c.p.f.u. in the Pb-source, as we have employed in our previous study (Beyer et al. 2019), the recrystallization process stalls.

Time Series

We conducted a time-series of experiments consisting of nine experiments run at a single temperature of 1118(2) °C with durations of 4 to 502 hours to study the evolution of this unusual diffusion – reaction system. With increasing time, we observed a monotonously increasing rim width (Figure 8 and Table 2). An indication of diffusion controlled, or at least affected, processes is that the length scale of transformation (reaction rim width, profile length, etc.) grows as the square root of time (i.e. a plot of length vs. square root of time is linear). We do see such linear trends in the data, but there are two distinct regimes - for experiments up to ~220 hours the apparent rate constant k is 3.65(14)E-8 m^2/s, whereas, the rate constant for experiments that lasted longer increased to 6.91(35)E-8 m^2/s (Figure 8). The error bars on the measured rim widths increase with run duration because the migrating interface becomes progressively wavier at longer times.

Temperature series

Seven experiments conducted between 753 and 1207 °C for 23 ½ hours each were used to determine the rates and activation energies of the diffusion - recrystallization process. To obtain

the rates of the above described reaction process, we assume that the slope representing the reaction rate at each temperature passes through the origin (Figure 8). This assumption is supported by the time series experiment at 1118 °C up to 220 hours, where the weighted linear fit passes through the origin. Thus, the experiments at different temperatures provide us a sense of how rates change with temperature (Table 3). For a diffusion controlled reaction the rate of growth of the reaction zone is proportional to an effective diffusion rate D and one has $x^2 \sim Dt$. The overall kinetics of growth of the reaction zone, k, is proportional to D and depends in addition on factors such as the geometry of the system and the Gibbs Free energy change of the reaction (ΔG) (see, for example, Wagner 1933), so that $x^2 = kt = \alpha Dt$, where the variable α includes the effects additional to D that enter in k. The temperature dependence of the process is controlled essentially by the temperature dependence of the effective Diffusion coefficient, D (the temperature dependence of quantities such as Gibbs free energy changes of reactions are very small in comparison). The diffusion coefficient D is expected to show an Arrhenius temperature dependence,

$$D = D_0 * e^{\frac{-E_A}{RT}} \quad (1)$$

with R representing the universal gas constant and the temperature T in Kelvin. We extracted the Arrhenius parameters for the composite transformation rate, k, from fits to plots of x^2 vs. t and constructed an Arrhenius plot for this quantity from where we obtained an activation energy (E_A) of 70(14) kJ/mol and pre-exponential factor (D_0 or k_0) of 1.79(0.84)E-05 m²/s (Figure 9). The activation energy for the diffusion - recrystallization process is substantially lower than the activation energies for lattice diffusion by either of the two possible mechanisms (~ 150 or ~ 130 kJ/mol) that were obtained by Beyer et al. (2019). This indicates that in spite of the influence of diffusion on the process, as seen in Figure 8, this coupled process has a lower activation barrier

and is hence more effective in causing chemical transformation compared to the process of diffusion alone.

Discussion

Relevant previous work to provide context to the results.

We investigated the effect of Pb-diffusion into $CaTiO_3$ single crystals (Beyer et al. 2019) using very similar experiments, with the only difference being that the concentration of Pb in the source was lower $Ca_{0.9}Pb_{0.1}TiO_3$. We found that at very low Pb concentrations in the crystal (10s – 100s µg/g Pb), i.e. low chemical gradient, Pb diffuses into the crystal via lattice diffusion. With increasing Pb concentration (> 1 mol% Pb), strain is induced into the relatively stiff lattice of $CaTiO_3$ due to the large difference between the ionic radii of Ca and Pb (Δr = 0.15 Å). That ultimately leads to the formation of planar defects and dislocations (cf. Figure 6 in Beyer et al. (2019)). It was observed that Pb begins to segregate in these defective regions, effectively getting "trapped" – it appears it is energetically favorable for the Pb-ions to segregate at the defects rather than migrate through the lattice against the lattice strain that is caused. Consequently, the diffusive flux of Pb through this region is reduced, resulting in lower diffusivities. As the concentration of Pb drops toward the interior of the crystal, Pb diffuses faster in the absence of the "trapping defects". Thus, there are two regions within the crystal that evolve with time – an exterior region with slow diffusion and an interior region with fast diffusion (these are clearly seen in the shapes of the concentration profiles) (Figure 10). Contrary to common expectation, in this case diffusion is slower in the defective region compared to that in the defect-free crystal.

Transport mechanism, energetics, and their implications

In this study, the driving force (i.e. chemical potential gradient) for the transport of Pb into the $CaTiO_3$ lattice was larger because the source was pure $PbTiO_3$. Consequently, the observed results may be explained by extension of the observations from our previous study as follows: It is reasonable to anticipate that a higher chemical potential difference would result in a larger flux of Pb into the $CaTiO_3$ single crystal and as a consequence that would result in the formation of a higher density of defective regions, where the Pb would tend to segregate. Once such a defect and Pb-rich region has formed, it should be energetically favorable to nucleate and form new, relatively defect-free crystals with grain boundaries (i.e. effectively, the planar defects migrate and coalesce to form grain boundary regions) rather than have a high density of dislocations / other planar defects because the surface energy is reduced by this process (e.g. Hackl and Renner 2013). These new grains would be Pb-rich, but the compositions of each of these grains are unlikely to be exactly the same, due to the slow diffusivity of Pb in $CaTiO_3$ (D_{Pb}^{slow} = 1.0(5)E-15 exp(-139(32) kJ/mol/RT) m^2/s (Beyer et al. 2019). This would result in the development of a lateral Pb-concentration heterogeneity, as is observed in the run products (Figure 3, Figure 5). Subsequently, Pb diffuses via the grain boundaries toward the interior, while simultaneously the newly formed grains also get enriched in Pb. Planar defects ultimately form in these as well and they go through the cycle of recrystallization once again. Thus, one creates a propagating front of a region of newly formed Pb-rich microcrystals that migrate into the interior of the $CaTiO_3$ single crystal with time. Ahead of this propagating front (termed "*migrating interface*" above), there is a region of low Pb-concentration where Pb-ions diffuse in the $CaTiO_3$ lattice via conventional point defect based diffusion mechanisms (as opposed to planar defects playing a significant role). This scenario explains the observations, including the coexistence of two different transport mechanisms (Regions I and III, separated by Region II) (Figure 5). The concentration of Pb at the transition between the zone with planar defects and the undisturbed crystal increased with time

This is the peer-reviewed, final accepted version for American Mineralogist, published by the Mineralogical Society of America.
The published version is subject to change. Cite as Authors (Year) Title. American Mineralogist, in press.
DOI: https://doi.org/10.2138/am-2021-7588. http://www.minsocam.org/

315 (Figure 7). This proposed mechanism and its different steps are illustrated schematically in
316 Figure 10.

317 From the perspective of energetics, the incorporation of Pb-ions into the $CaTiO_3$ lattice is
318 driven by the chemical potential difference between the source and the single crystal. In the
319 $CaTiO_3$ crystal the available energy is partitioned into two components – lattice strain that results
320 from the size mismatch between the sizes of Pb and Ca ions counters the incorporation of Pb into
321 the lattice, and diffusive flux that transports Pb into the interior of the crystal helps to dissipate
322 the build-up of strain and facilitate the incorporation of more Pb-ions into the lattice. The lattice-
323 strain depends on parameters such as the bulk modulus (and other elastic constants) of the crystal
324 and the extent of size mismatch, while the diffusive flux depends on parameters such as the
325 number of available point defects and the dynamics of ionic jump frequencies. Clearly, new
326 planar defects are formed when a certain threshold of elastic strain is exceeded. These, in turn,
327 affect the local chemical potential and favor the accumulation of Pb-ions in these regions rather
328 than in the strained lattice (e.g. see Figure 9 and Beyer et al. 2019). It is also possible for the
329 planar defects to migrate and merge, in order to reduce available interfaces, and organize
330 themselves into grain boundaries that delineate relatively planar defect-free microcrystals. Such
331 migration of interfaces and grain-boundaries driven by chemical forces happens, for example,
332 during chemically induced grain boundary migration (CIGM) which is a well-known
333 phenomenon in materials sciences (e.g. Cahn et al. 1979; Balluffi and Cahn 1981; Hillert 2004)
334 and has also been observed in rock forming minerals such as calcite (Evans et al. 1986; Hay and
335 Evans 1987). Thus, the ultimate distribution of Pb in the $CaTiO_3$ single crystal depends on the
336 energetic balance between lattice strain effects, the generation of new discontinuities in the
337 crystal in the forms of planar defects or grain boundaries, and the migration of Pb into the crystal.
338 This intimate interplay between chemical and mechanical forces and the phenomena that result

339 from this in an oxide type material (i.e. not purely ionic or metallic) is a novel finding of this
340 study. The discovery has several very significant implications:

341 (i) Chemical differences influence mechanical deformation (formation of planar defects,
342 recrystallization) and vice versa (availability of defects leads to "pinning" of Pb at
343 these sites and reduction of flux of Pb). These is a "give and take" between chemical
344 and mechanical controls and the energetic balance between these governs the overall
345 evolution. It is commonly perceived and observed that deformation enhances
346 diffusion and/or chemical reaction (e.g. Urai et al. 1986; Yund and Tullis 1991). In
347 the novel mode of transport observed here, deformation *affects but does not*
348 *necessarily enhance* chemical reaction and diffusion is in fact *slowed down* through
349 the presence of the planar defects.

350 (ii) One has diffusion profiles as well as a discontinuous concentration jump, typically
351 taken to be a signature of dissolution-precipitation reactions, in the same system,
352 simultaneously, and in a continually evolving manner. This has major implications
353 for petrological applications, as discussed below. Notably, the simple binary
354 distinction between "diffusion-control" vs. "reaction-control" reactions does not
355 apply to such systems, as has been shown in other situations as well (e.g. Dohmen
356 and Chakraborty 2003).

357 (iii) The newly formed grains are chemically zoned (or become chemically zoned as the
358 process evolves), and their composition evolves with time – it is noteworthy that they
359 are not of the final equilibrium composition that is expected at the pressure and
360 temperature conditions of the experiment. Again, this has major implications for
361 petrological applications that are discussed in the following section.

This is the peer-reviewed, final accepted version for American Mineralogist, published by the Mineralogical Society of America.
The published version is subject to change. Cite as Authors (Year) Title. American Mineralogist, in press.
DOI: https://doi.org/10.2138/am-2021-7588. http://www.minsocam.org/

(iv) The activation energy of the overall process is different from that of diffusion (>130 kJ/mol, see Beyer et al. 2019) or the free energy change involved in the transformation of $CaTiO_3$ to a Pb-rich composition (ΔG of reaction is of the order of several kJ/mol). Specifically, through the coupling of chemical and mechanical processes, it is a more efficient means of chemical transformation than either volume- or grain-boundary diffusion or simple chemical replacement by themselves. Thus, it is a previously undiscovered, coupled process that would lead to its own kinetics and temperature- or time-dependence. A consequence will be that new values of geochemically relevant parameters such as closure temperatures are expected (see below).

(v) A fundamental thermodynamic implication is that in addition to conventional conjugate variables such as (S,T), (P,V) and (μ_i,n_i), we need to consider surface energetics as well, through (Γ_i, A_i) where Γ_i is a surface / interface free energy term and A_i is the relevant surface area:

$$\Delta G = -SdT + VdP + \sum \mu_i dn_i + \Gamma dA_i \quad (2)$$

Usually, only the first three terms on the right hand side are considered. Note that one can change Γ_i by changing the material in the surrounding environment (e.g. presence / absence of melt / fluids – see example below) and area by processes such as fracturing, other forms of deformation (leading to, for example, recrystallization and new grain growth - Urai et al. 1986), or chemical processes such as the ones studied here.

Geological consequences

Petrological implications

In reading the rock record, chemical signatures are used to infer the temperatures, pressures, or other intensive thermodynamic variables related to properties such as the oxidation state or water content of a system. Modern petrology has shifted from asking the question "at what condition did the rock form?" to a more process oriented view where one asks "what *conditions* did the rock experience?", and the related question, "what stages of the process(es) seen by the rock are recorded and preserved in the rock?" Equilibrium thermodynamics has been used very gainfully to address these questions. However, if crystals grow and dissolve several times in the course of their evolution, it is clear that the record from only the last of these episodes can be read from the signatures in the rock. Thus, important as it is to determine, for example, the correct temperatures or pressures recorded in the chemistry of minerals in a rock, it is perhaps even more important to recognize what stage in the evolutionary history of the rock those pressure and temperature conditions relate to.

We can illustrate this aspect using two examples. A metamorphic rock that evolved along a clockwise P-T path may have formed a key mineral such as garnet at the P-T condition where the stability field of garnet was crossed for the first time. During subsequent evolution, the composition of the garnet may readjust, by processes such as diffusion, up to the peak P-T condition and this may be recorded in the chemistry of the garnet. However, there are instances where it may be shown that diffusion timescales were not sufficient to adjust the composition of large garnet grains completely, and moreover, the nature of inclusions in the garnet indicate that the entire grain grew at conditions corresponding to a certain P-T region of a phase diagram. One such example is shown in Figure 11, which illustrates a garnet grain from the higher Himalayan crystallines in the eastern Himalayan range from the state of Sikkim, India. This is from one of

the rocks (TG 8D-03) studied by Sorcar et al. (2014), where detailed petrological information on the rock may be found. The entire grain contains polyphase inclusions of quartz + feldspar (plagioclase /K-feldspar) +/- biotite +/- accessory phases which have been interpreted to be crystallized melts (e.g. "nanogranites" according to the definition of Cesare et al. (2009). The observation suggests that the grains that are being observed now crystallized entirely in the presence of melt at T > 700 °C, even though garnet as a phase should have been stable in these pelitic rocks at T ~ 500 °C along its prograde history. Based on the observations of this study, we feel it is quite likely that garnet grains have evolved by diffusion as well as recrystallization and the grains that are being observed today are the ones that are the products of the last phase of such recrystallization. Without the insights from this study, a reasonable inference could be that even though garnet should have been stable at ~ 500 °C it did not form until the rock crossed 700 °C in its P-T evolution i.e. that growth of garnet was highly overstepped and under disequilibrium conditions. These two interpretations have very different implications for our understanding of metamorphic rocks and processes. The examples underscore the need for quantifying not only the conventional Gibbs free energy of a system, but also the terms involving (Γ_i, A_i) which would also allow the textural maturation process, as shown in the equation 2. Textural maturation includes the disappearance of older grains and appearance and growth of new ones, accompanied by changes in size and shape, even when the grains may have been in chemical equilibrium.

A second example relates to igneous systems. Olivines in many basaltic systems, for example in the study of Kahl et al. (2015) from Mt. Etna, record conditions from the crustal magma reservoirs. However, an analysis of their phase relations suggest that olivine is a liquidus phase that would have been stable in the melt through its entire history beginning with extraction from the mantle source region. Now, in these high temperature systems it is possible that

diffusion modified the chemical compositions of the crystals completely during their transit from the mantle through the crust to eruption. However, there are also indications that particularly for some slowly diffusing elements, and given the timescales of evolution, this would not have been feasible. The results from this study provide an alternative possibility that should be explored – the olivine grains may have gone through many phases of dissolution and new growth in the course of evolution of the system, and the grains we find today are the ones from the last phase of such growth in a crustal magma chamber.

Implications for Geochemistry and Geochronology

The considerations discussed above apply to geochemical and geochronological studies as well. The interpretation of trace element signatures, and in particular the dates obtained from specific minerals (e.g. zircons, garnets), depend completely on what we infer the time of growth of the crystal to be. For example, garnets from the region mentioned above (Sikkim, E. Himalaya) were dated by Anczkiewicz et al (2014) by the Lu-Hf method. Garnets from the Higher Himalayan crystallines, such as the one considered above, showed weak to no zoning profiles of REE elements (e.g. Lu) and the dates obtained from them were interpreted to be dates of peak metamorphism in the presence of melt. On the other hand, from the same region but a range of lower grades (garnet zone to kyanite zone), garnets showed strongly zoned REE profiles with the Lu concentrated essentially at the core of the garnet. The P-T determinations also showed garnet to have commenced growth at ~500 °C, as thermodynamic equilibrium would predict (e.g. Gaidies et al. 2015; George and Gaidies 2017). Thus, the dates obtained from these garnets, using the same isotopic system – Lu-Hf, were interpreted to be the dates of first garnet

454 growth during prograde metamorphism rather than peak metamorphism. Similar considerations
455 apply to other minerals used for geochronology (e.g. zircons, monazites) – see, for example,
456 Rubatto et al. (2013) for an example of how dates from zircons and monazites can be related to
457 specific phases of growth of these crystals at specific stages of the metamorphic cycle of a rock.
458 Thus, it is important to consider when specific grains (or parts of grains) grew in order to be able
459 to assign the geochronological results properly to physical events during the evolution of a rock.

460

461

462

463 **Implications for Geodynamics**

464 A consideration that has become a considerably hotly debated issue is the extent to which a
465 mineral grain may record tectonic overpressures during its evolution (e.g. Schmalholz and
466 Podladchikov 2014; Moulas et al. 2019). The key question in that debate is whether pressures
467 obtained using barometry can be converted to depth of burial directly, or whether these pressures
468 may record internal stresses in the system, which may be considerably in excess of that due to the
469 lithostatic pressure at a given depth of burial. These analyses and mathematical models are
470 carried out using continuum methods. However, as seen in this study, crystals may respond to the
471 development of strain by the formation of discontinuities such as planar defects or grain
472 boundaries, which act as a means of releasing stress, and may lead to recrystallization. Thus, such
473 considerations need to be considered in the debate on tectonic overpressures to get realistic
474 estimates.

475 **Implications for Geospeedometry and Diffusion chronometry**

Geospeedometry and diffusion chronometry relies on the measurement and modeling of concentration gradients formed by diffusion to obtain information on timescales (e.g. durations of events, residence times of magmas, cooling rates or exhumation rates). Again, thermodynamic relations (e.g. phase diagrams, thermobarometry) are used to infer when a mineral formed and the timescale that is obtained by modelling concentration profiles is the time spent by the rock between that temperature up to the point when the diffusing system closed. However, consider the observations in the system studied in this work. The newly formed microcrystals are zoned, but they form at different times, and their shapes and sizes evolve during the evolution of the system. Modelling the zoning profile in one of those crystals would yield only the timescale during which that given crystal existed, and not the evolution of the whole system. Similarly, modelling the zoning profile in Region III would yield the timescale from the point of time when the front (Region II) reached its current position, and not the timescale of the overall evolution of the system. Thus, it is important to understand the evolution of such complex coupled systems in order to be able to interpret timescales obtained from diffusion modelling suitably.

Additionally, as noted above, the temperature at which a system freezes (= closure temperature) depends strongly on the activation energy of the relevant kinetic process (Dodson 1973). As the activation energy for such a coupled process has been shown to be considerably different from the activation energy of the purely diffusive process (see above), it follows that the closure temperature of the system would also be considerably different compared to that obtained from the consideration of diffusion rates only. This would also, additionally, affect the interpretation of timescales obtained from modelling concentration profiles in such systems.

Finally, the shapes of the profiles formed by these coupled processes do not necessarily follow a standard error-function shape and more complex models would be required to fit these profiles.

Thus, on the whole, this study shows that chemical potential gradients can drive diffusive fluxes as well as deformation and recrystallization processes, and that these occur in parallel. This has far reaching consequences for petrological and geochemical interpretations of the rock record, some of which have been discussed above.

Acknowledgments

We thank N. Jöns for assistance with the microprobe and R. Dohmen for fruitful discussions. We also thank J. Berndt for access to the LA-ICP-MS setup at the Institute of Mineralogy, University of Münster. The handling editor T. Müller and the reviewers E.B. Watson and J. Wheeler are thanked for their detailed and helpful reviews that helped us to greatly improve the manuscript.

References

Anczkiewicz, R., Chakraborty, S., Dasgupta, S., Mukhopadhyay, D., and Ko\ltonik, K. (2014) Timing, duration and inversion of prograde Barrovian metamorphism constrained by high resolution Lu–Hf garnet dating: A case study from the Sikkim Himalaya, NE India. Earth and Planetary Science Letters, 407, 70–81.

Balluffi, R.W., and Cahn, J.W. (1981) Mechanism for diffusion induced grain boundary migration. Acta metallurgica, 29, 493–500.

Beyer, C., Dohmen, R., Rogalla, D., Becker, H.-W., Marquardt, K., Vollmer, C., Hagemann, U., Hartmann, N., and Chakraborty, S. (2019) Lead diffusion in $CaTiO_3$: A combined study using Rutherford backscattering and TOF-SIMS for depth profiling to reveal the role of lattice strain in diffusion processes. American Mineralogist, 104, 557–568.

Cahn, J.W., Pan, J.D., and Balluffi, R.W. (1979) Diffusion induced grain boundary migration. Massachusetts Inst. of Tech., Cambridge (USA).

Cesare, B., Ferrero, S., Salvioli-Mariani, E., Pedron, D., and Cavallo, A. (2009) "Nanogranite" and glassy inclusions: The anatectic melt in migmatites and granulites. Geology, 37, 627–630.

Chandra, A., and Pandey, D. (2011) Evolution of crystallographic phases in the system $(Pb_{1-x}Ca_x)TiO_3$: A Rietveld study. Journal of Materials Research, 18, 407–414.

Dodson, M.H. (1973) Closure temperature in cooling geochronological and petrological systems. Contributions to Mineralogy and Petrology, 40, 259–274.

Dodson, M.H., Gledhill, A.R., Shackleton, R.M., and Bell, K. (1975) Age differences between Archaean cratons of eastern and southern Africa. Nature, 254, 315–318.

Dohmen, R., and Chakraborty, S. (2003) Mechanism and kinetics of element and isotopic exchange mediated by a fluid phase. American Mineralogist, 88, 1251–1270.

Essene, E.J. (1982) Geologic thermometry and barometry. Reviews in Mineralogy and Geochemistry, 10, 153–206.

Evans, B., Hay, R.S., and Shimizu, N. (1986) Diffusion-induced grain-boundary migration in calcite. Geology, 14, 60–63.

Gaidies, F., Petley-Ragan, A., Chakraborty, S., Dasgupta, S., and Jones, P. (2015) Constraining the conditions of Barrovian metamorphism in Sikkim, India: P–T–t paths of garnet crystallization in the Lesser Himalayan Belt. Journal of Metamorphic Geology, 33, 23–44.

George, F.R., and Gaidies, F. (2017) Characterisation of a garnet population from the Sikkim Himalaya: insights into the rates and mechanisms of porphyroblast crystallisation. Contributions to Mineralogy and Petrology, 172, 57.

Griffin, W.L. (2008) GLITTER: data reduction software for laser ablation ICP-MS. Laser Ablation ICP-MS in the Earth Sciences: Current practices and outstanding issues, 308–311.

Hackl, K., and Renner, J. (2013) High-temperature deformation and recrystallization: A variational analysis and its application to olivine aggregates. Journal of Geophysical Research: Solid Earth, 118, 943–967.

Hay, R.S., and Evans, B. (1987) Chemically induced grain boundary migration in calcite: temperature dependence, phenomenology, and possible applications to geologic systems. Contributions to Mineralogy and Petrology, 97, 127–141.

Hillert, M. (2004) Solute drag in grain boundary migration and phase transformations. Acta materialia, 52, 5289–5293.

Jonas, L., Müller, T., Dohmen, R., Baumgartner, L., and Putlitz, B. (2015) Transport-controlled hydrothermal replacement of calcite by Mg-carbonates. Geology, 43, 779–782.

Kahl, M., Chakraborty, S., Pompilio, M., and Costa, F. (2015) Constraints on the nature and evolution of the magma plumbing system of Mt. Etna volcano (1991–2008) from a combined thermodynamic and kinetic modelling of the compositional record of minerals. Journal of Petrology, 56, 2025–2068.

Lasaga, A.C. (1983) Geospeedometry: an extension of geothermometry. In Kinetics and equilibrium in mineral reactions pp. 81–114. Springer.

Lasaga, A.C., Richardson, S.M., and Holland, H.D. (1977) The mathematics of cation diffusion and exchange between silicate minerals during retrograde metamorphism. In Energetics of geological processes pp. 353–388. Springer.

Merlet, C. (1994) An accurate computer correction program for quantitative electron probe microanalysis. Microchimica Acta, 114, 363–376.

Moulas, E., Schmalholz, S.M., Podladchikov, Y., Tajčmanová, L., Kostopoulos, D., and Baumgartner, L. (2019) Relation between mean stress, thermodynamic, and lithostatic pressure. Journal of metamorphic geology, 37, 1–14.

Patterson, C. (1956) Age of meteorites and the earth. Geochimica et Cosmochimica Acta, 10, 230–237.

Ramberg, H., and DeVore, G. (1951) The distribution of Fe^{++} and Mg^{++} in coexisting olivines and pyroxenes. The Journal of Geology, 59, 193–210.

Rubatto, D., Chakraborty, S., and Dasgupta, S. (2013) Timescales of crustal melting in the Higher Himalayan Crystallines (Sikkim, Eastern Himalaya) inferred from trace element-constrained monazite and zircon chronology. Contributions to Mineralogy and Petrology, 165, 349–372.

582 Schmalholz, S.M., and Podladchikov, Y. (2014) Metamorphism under stress: The problem of
583 relating minerals to depth. Geology, 42, 733–734.

584 Sorcar, N., Hoppe, U., Dasgupta, S., and Chakraborty, S. (2014) High-temperature cooling
585 histories of migmatites from the High Himalayan Crystallines in Sikkim, India: rapid
586 cooling unrelated to exhumation? Contributions to Mineralogy and Petrology, 167, 957.

587 Tappe, S., and Simonetti, A. (2012) Combined U–Pb geochronology and Sr–Nd isotope analysis
588 of the Ice River perovskite standard, with implications for kimberlite and alkaline rock
589 petrogenesis. Chemical Geology, 304, 10–17.

590 Tera, F., and Wasserburg, G.J. (1972) U-Th-Pb systematics in lunar highland samples from the
591 Luna 20 and Apollo 16 missions. Earth and Planetary Science Letters, 17, 36–51.

592 Urai, J.L., Means, W.D., and Lister, G.S. (1986) Dynamic recrystallization of minerals. In
593 Mineral and rock deformation: laboratory studies Vol. 36, pp. 161–199. AGU
594 Washington, DC.

595 Urey, H.C., Lowenstam, H.A., Epstein, S., and McKinney, C.R. (1951) Measurement of
596 paleotemperatures and temperatures of the Upper Cretaceous of England, Denmark, and
597 the southeastern United States. Geological Society of America Bulletin, 62, 399–416.

598 Wagner, C. (1933). Beitrag zur theorie des anlaufvorgangs. Zeitschrift für physikalische Chemie,
599 21(1), 25-41.

600 Walther, J.V., and Wood, B.J. (1984) Rate and mechanism in prograde metamorphism.
601 Contributions to Mineralogy and Petrology, 88, 246–259.

602 Wetherill, G.W. (1956) Discordant uranium-lead ages, I. Eos, Transactions American
603 Geophysical Union, 37, 320–326.

604 Yund, R.A., and Tullis, J. (1991) Compositional changes of minerals associated with dynamic
605 recrystallizatin. Contributions to Mineralogy and Petrology, 108, 346–355.

606

607

608

609

610

611

612

613

614 **Captions**

615 **Table 1** Representative major element (wt.% oxides) and trace element concentration (μg/g)
616 in the natural perovskite crystals, measured with EMPA and LA-ICP-MS.

617

618 **Table 2** Experimental conditions of the annealing of natural $CaTiO_3$ single crystals embedded in
619 $PbTiO_3$ powder contained in a Pt capsule welded shut.

620 **Table 3** Results of fitting rate constants to the experimental data and the corresponding Arrhenius
621 equation. [a] uncertainty is set to 0.2 log units because the reaction rate is extracted from a two-
622 point curve, see Figure 8.

623 **Figure 1** Powder diffraction pattern (Cu radiation) of the synthetic starting material $PbTiO_3$,
624 synthesized with an excess of PbO, to account for Pb-loss during the experimental anneal.
625 Reflections of $PbTiO_3$ are labelled. We also observed minor PbO (111 reflection labelled in the
626 figure) but no unreacted TiO_2.

627 **Figure 2** BSE image of experiment Pv_Pb_D3 run at 1118 °C for 118.5 h. The original surface is
628 marked by a layer of apatite crystal (dark grey). The recrystallized rim is composed of
629 $(Pb,Ca)TiO_3$ solid solutions (light grey). The white circles represent Pt-wire that were wrapped
630 around the untreated single crystals to mark the surface.

631 **Figure 3** Back-scattered electron image of sample Pv_Pb_D3 run at 1118 °C for 118.5 h showing
632 the internal zonation of the solid solution grains and the undulated morphology of the migrated
633 interface. Brighter regions contain larger concentrations of Pb. The red box marks the area from

which the 3d surface plot was created. The colored height information (z) is extracted from the greyscale.

Figure 4 a) Band contrast and grain orientation map of one section of experiment Pv_Pb_D4 **(**1118 °C, 166 ¼ h.). The color coding corresponds to the orientation parallel to Z. b) Inverse pole figures parallel showing the orientation of the $CaTiO_3$ single crystal and the recrystallized rim parallel to the three major axis. Clusters of higher intensity represent the single crystal substrate and the diffuse areas are representative of the grain orientation in the rim (see a). c) Relative distribution of the grain perimeters. The rim is composed of grains with perimeters between 0 and 135 μm. We observed no apparent clustering around a certain value.

Figure 5 Illustration of the different regions of the observed processes and the characteristic features as described in the text, based on a BSE image of experiment Pv_Pb_D4. Note that the presence of Pb in the diffusive region (III) is not detectable with Z-contrast imaging-

Figure 6 Maximum concentration of Pb (in cations per formula unit) at the original interface as a function of experimental duration in hours. With variation parallel to the migrating interface in mind (see text for discussion) the maximum concentration of Pb in the solid solutions at the $PbTiO_3$ interface increases with prolonged run times.

Figure 7 Pb concentration in cations per formula unit (c.p.f.u.) as a function of distance from the migrating interface. All experiments were carried out at 1118 °C. The striped area represents the range of compositions at which the discontinuous jump in concentration occurs in experiments of different duration.

Figure 8 Measured width of the newly grown rim shown as a function of the square root of time. The broken lines are drawn under the assumption that the lines pass the origin. The solid line is a weighted fit of the experiments conducted at 1118 °C that lasted longer than 220 hours.

Figure 9 Arrhenius diagram showing the apparent rate constant k against temperature. We calculated the slope with an error of at least 0.2 log unit on each datum to reflect the uncertainties related to our assumptions, which are discussed in the text. For the datapoint at 1118 °C we calculated the uncertainty to be 0.06 log units.

Figure 10 Series of images that illustrate the evolution of a dynamically recrystallizing interface as discussed in the text. (left image) After the formation of defects just below the crystal surface due the chemical potential gradient imposed by $PbTiO_3$ (X), Pb segregates into the defect rich region and forms a second interface between the defect rich region and the undisturbed $CaTiO_3$ single crystal (middle image). The lower chemical potential between these two regions facilitates the diffusion of Pb by point defects. If the chemical potential is high enough, the linear/plane defects merge and form grain boundaries to dissipate the excess energy that is generated of pinning Pb ions to the defects. The stripped insert in the right image represents the diffusion profile of Pb in the single crystal as we have observed in our previous study (Beyer et al. 2019). The insert is exaggerated to highlight the profile shape.

Figure 11 Microphotograph of a garnet crystal from the High Himalayan Crystallines in the greater Himalayan sequence in Sikkim, E. India under crossed polars. This sample (TG 8D-03) comes from a migmatitic gneiss with the main assemblage of quartz - plagioclase - K-feldspar - garnet - sillimanite (rarely kyanite) - biotite (+/- cordierite and/or spinel). The detailed petrographic features of this and other similar samples from the unit may be found in Sorcar et al. (2014). (a) Note the light spots (inclusions) against the dark background of the garnet. (b) A close

677 up of one of the larger such inclusions, showing that it is multiphase in nature, consisting in this
678 case of quartz - plagioclase - biotite. The other inclusions studied under a SEM reveal similar
679 multiphase assemblages.

680 **Tables**

681 **Table 1**

Element	mean (n = 6)	uncertainty		
P_2O_5	0.57	0.02		
TiO_2	58.50	0.09		
CaO	40.92	0.13		
	crystal 1 (n = 15)	uncertainty	crystal 2 (n = 9)	uncertainty
Na	28	1	33.9	0.2
Si	190	7	199.0	2.1
Sc	0.294	0.004	0.701	0.003
Fe*	2806	1509	8252	3633
Rb	0.218	0.003	0.356	0.001
Sr	22	0	21.3	0.1
Y	1181	13	2007.0	6.6
Zr	30.4	0.3	21.8	0.1
Nb	169	2	156.0	0.5
Cs	bdl		bdl	
Ba	0.185	0.005	0.174	0.001
La	318	4	904	4
Ce	942	15	1974	10
Pr	135	2	240	1
Nd	584	11	967	6
Sm	155	3	234	2
Eu	66	1	72.2	0.4
Gd	192	4	273	2
Tb	33	1	47.3	0.4
Dy	219	4	317	2
Ho	46	1	71	1
Er	121	3	204	2
Tm	14.4	0.4	27.3	0.3
Yb	77	2	166	1
Lu	8.6	0.2	19.8	0.2
Hf	1.45	0.03	2.72	0.02
Ta	8.9	0.2	10.9	0.1
Pt	bdl		bdl	
Pb	9.7	0.3	14.2	0.1
Th	30	1	154	2
U	14.2	0.4	15.2	0.1
Total	7402		16406	

bdl: below detection limit, *low signal to noise ratio

Note the major elements were measured after the diffusion experiment. The trace element concentration was measured on untreated crystal fragments.

682

This is the peer-reviewed, final accepted version for American Mineralogist, published by the Mineralogical Society of America.
The published version is subject to change. Cite as Authors (Year) Title. American Mineralogist, in press.
DOI: https://doi.org/10.2138/am-2021-7588. http://www.minsocam.org/

683 **Table 2**

sample name	duration [h]	T [°C]	rim width [µm]	uncertainty [µm]	notes
Pv_Pb_D1	4	1118	4.5	1.5	partial Pb-loss
Pv_Pb_D2	23.5	1118	9	3	
Pv_Pb_D3	118.5	1118	23.5	4	
Pv_Pb_D4	166.25	1118	30	6	partial Pb-loss
Pv_Pb_D5	286.75	1118	44	8	partial Pb-loss
Pv_Pb_D6	23.5	753	1.5	1	
Pv_Pb_D7	23.5	931	5	2	
Pv_Pb_D8	23.5	1207	32	5	
Pv_Pb_D9	69	1118	n.d.		Pb-loss
Pv_Pb_D10	216	1118[a]	36	3	short drop in furnace temperature to 760 °C (< 30 minutes)
Pv_Pb_D11	336	1118	53	6	
Pv_Pb_D12	502	1118	68	8	

684

This is the peer-reviewed, final accepted version for American Mineralogist, published by the Mineralogical Society of America.
The published version is subject to change. Cite as Authors (Year) Title. American Mineralogist, in press.
DOI: https://doi.org/10.2138/am-2021-7588. http://www.minsocam.org/

685 **Table 3**

T [°C]	ln(k) [m²/s]
1207	-16.11(20[a])
1118	-17.14(6)
931	-17.72(20 [a])
753	-19.11(20 [a])

Arrhenius equation

$\ln(k_0)$ [m²/s]	E_A [kJ/mol]
-11(1)	70(14)

686

This is the peer-reviewed, final accepted version for American Mineralogist, published by the Mineralogical Society of America.
The published version is subject to change. Cite as Authors (Year) Title. American Mineralogist, in press.
DOI: https://doi.org/10.2138/am-2021-7588. http://www.minsocam.org/

687 **Figures**

688 **Figure 1**

689

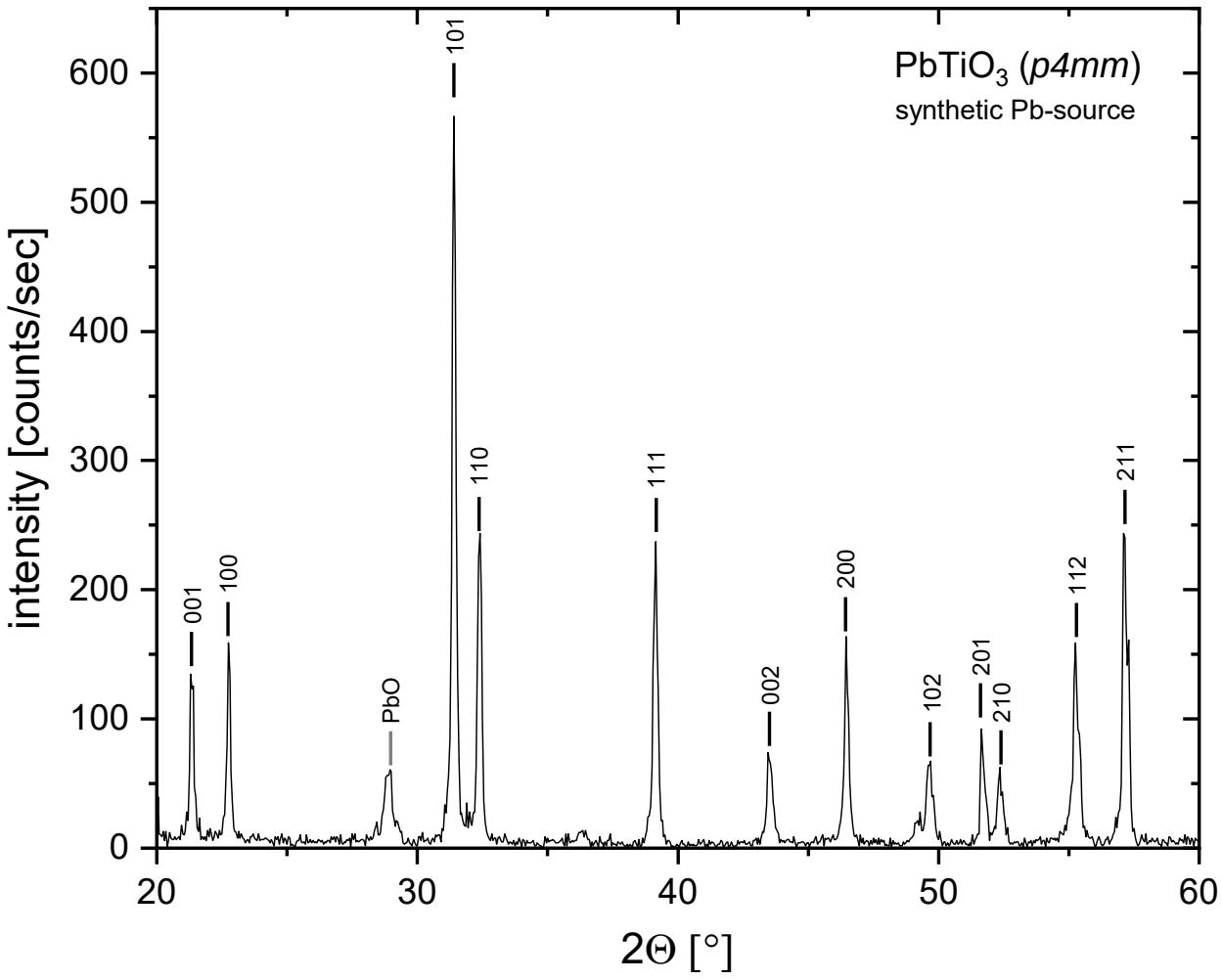

690

691

692

693

694

695

This is the peer-reviewed, final accepted version for American Mineralogist, published by the Mineralogical Society of America.
The published version is subject to change. Cite as Authors (Year) Title. American Mineralogist, in press.
DOI: https://doi.org/10.2138/am-2021-7588. http://www.minsocam.org/

696 **Figure 2**

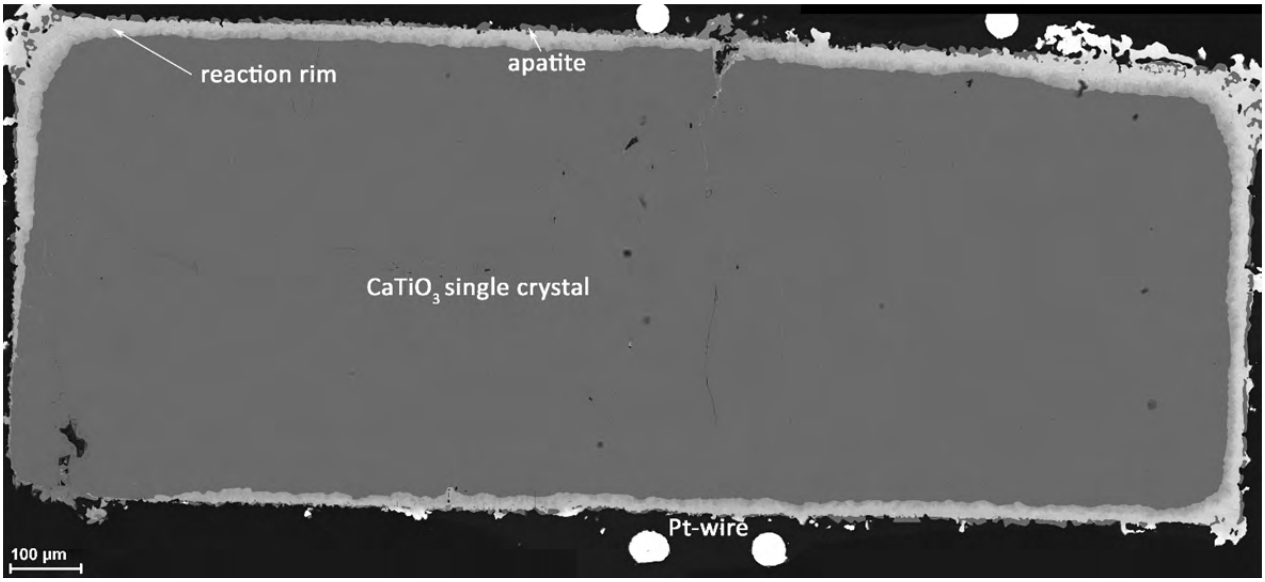

697

698

This is the peer-reviewed, final accepted version for American Mineralogist, published by the Mineralogical Society of America.
The published version is subject to change. Cite as Authors (Year) Title. American Mineralogist, in press.
DOI: https://doi.org/10.2138/am-2021-7588. http://www.minsocam.org/

699 **Figure 3**

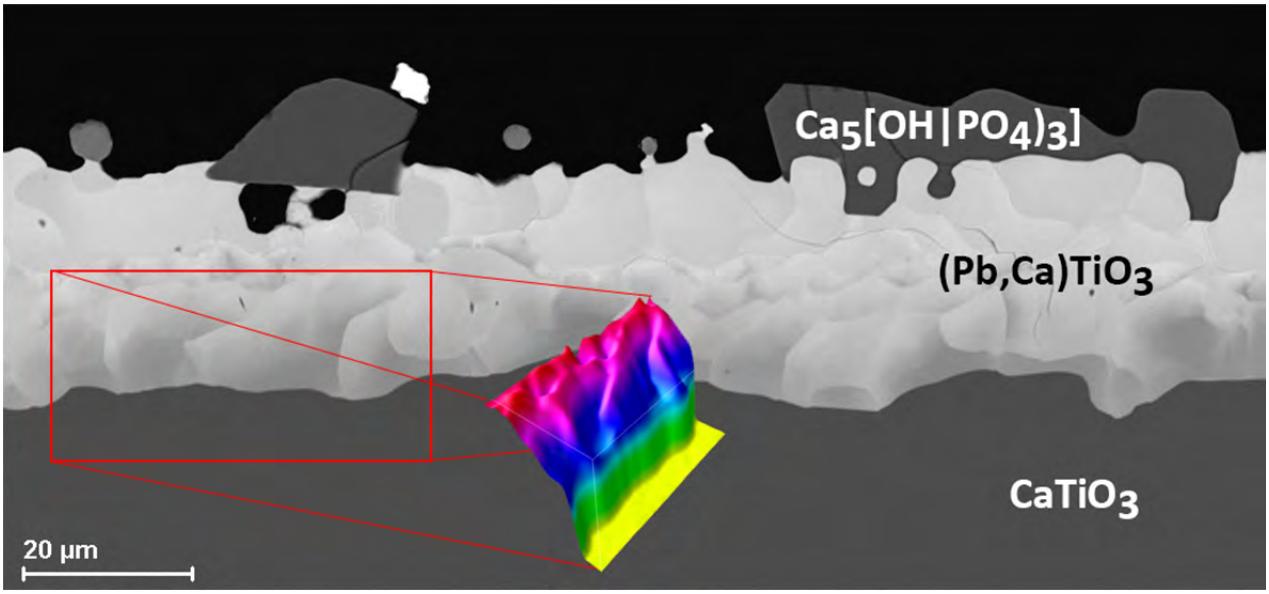

700

701

This is the peer-reviewed, final accepted version for American Mineralogist, published by the Mineralogical Society of America.
The published version is subject to change. Cite as Authors (Year) Title. American Mineralogist, in press.
DOI: https://doi.org/10.2138/am-2021-7588. http://www.minsocam.org/

Figure 4

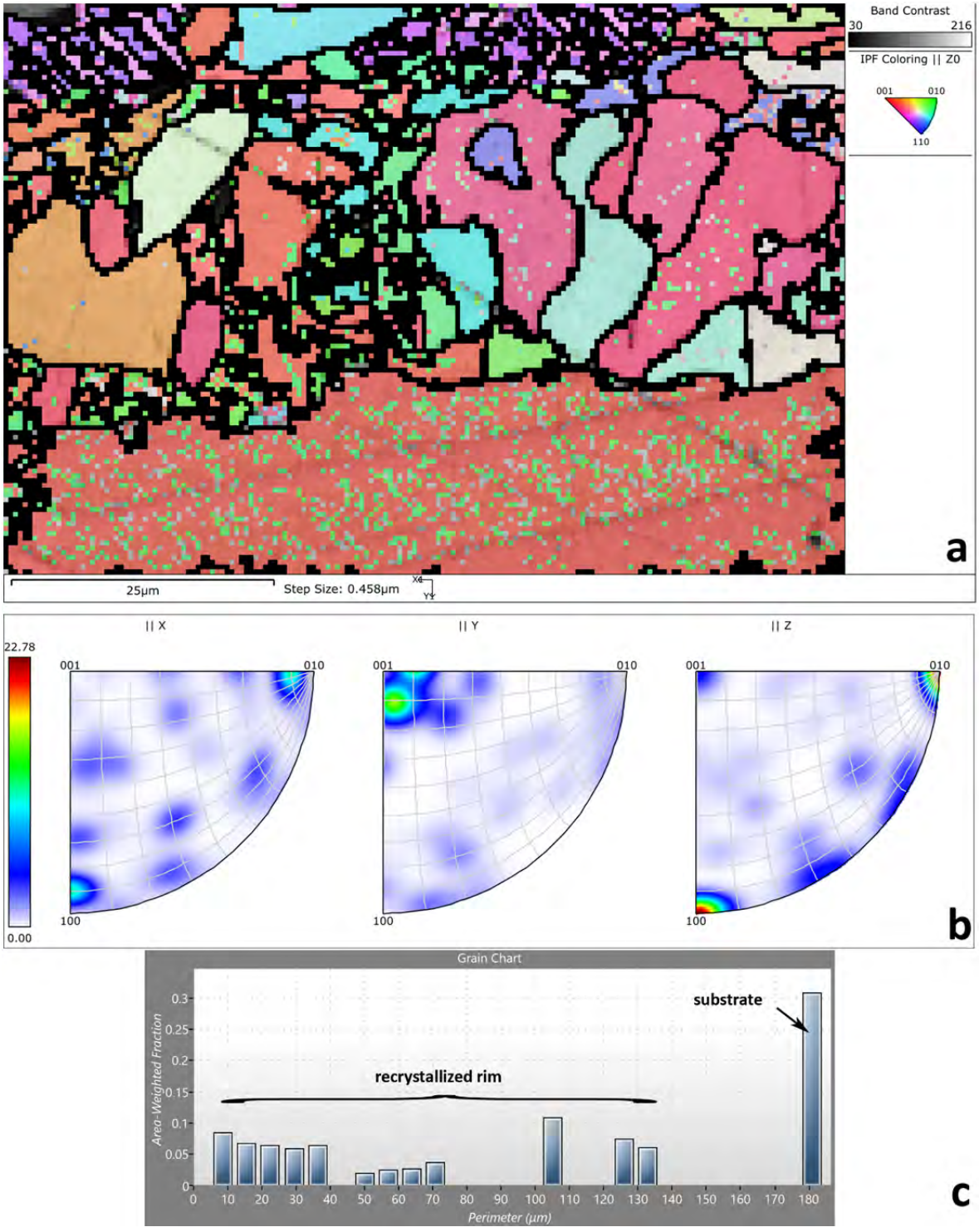

This is the peer-reviewed, final accepted version for American Mineralogist, published by the Mineralogical Society of America.
The published version is subject to change. Cite as Authors (Year) Title. American Mineralogist, in press.
DOI: https://doi.org/10.2138/am-2021-7588. http://www.minsocam.org/

705 **Figure 5**

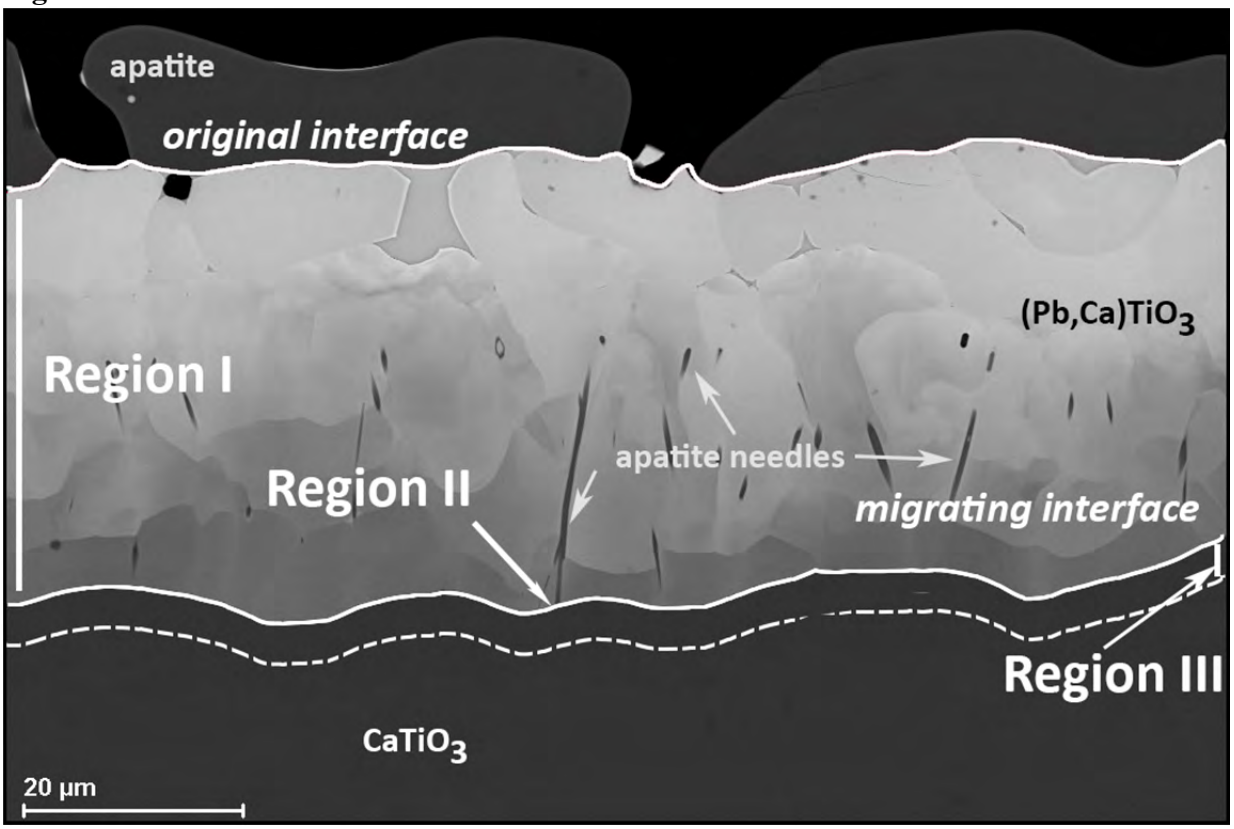

706

This is the peer-reviewed, final accepted version for American Mineralogist, published by the Mineralogical Society of America.
The published version is subject to change. Cite as Authors (Year) Title. American Mineralogist, in press.
DOI: https://doi.org/10.2138/am-2021-7588. http://www.minsocam.org/

707 **Figure 6**

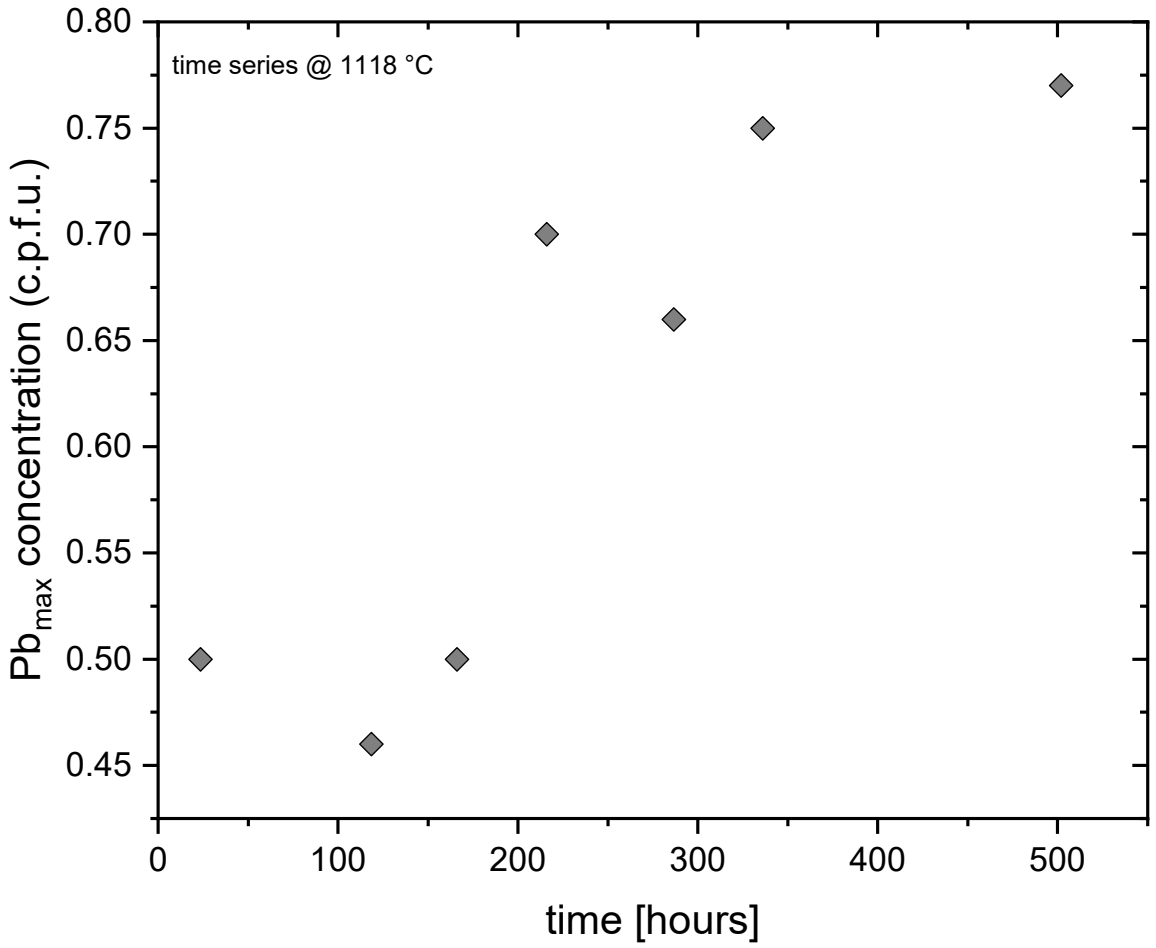

708

709

This is the peer-reviewed, final accepted version for American Mineralogist, published by the Mineralogical Society of America.
The published version is subject to change. Cite as Authors (Year) Title. American Mineralogist, in press.
DOI: https://doi.org/10.2138/am-2021-7588. http://www.minsocam.org/

710 **Figure 7**

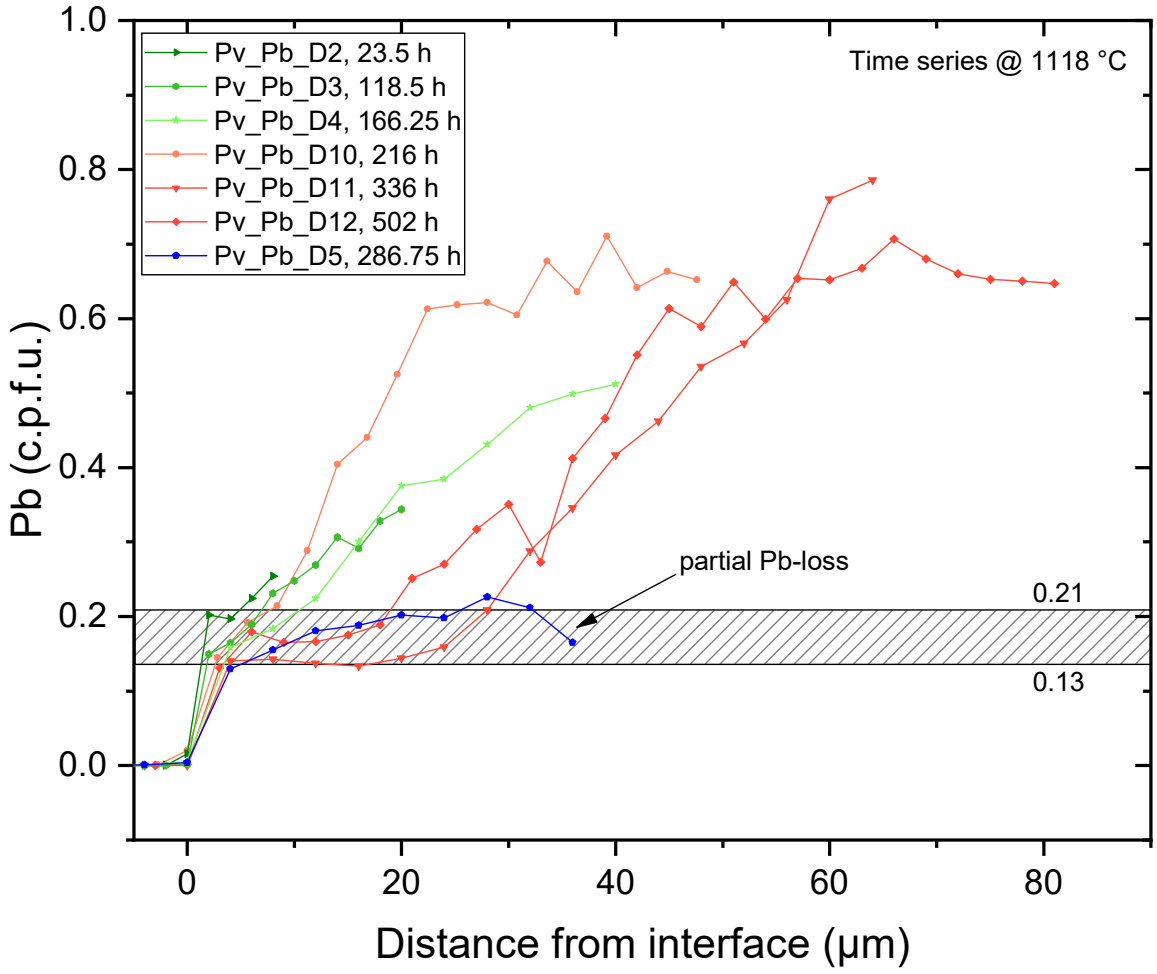

711

712

This is the peer-reviewed, final accepted version for American Mineralogist, published by the Mineralogical Society of America.
The published version is subject to change. Cite as Authors (Year) Title. American Mineralogist, in press.
DOI: https://doi.org/10.2138/am-2021-7588. http://www.minsocam.org/

713 **Figure 8**

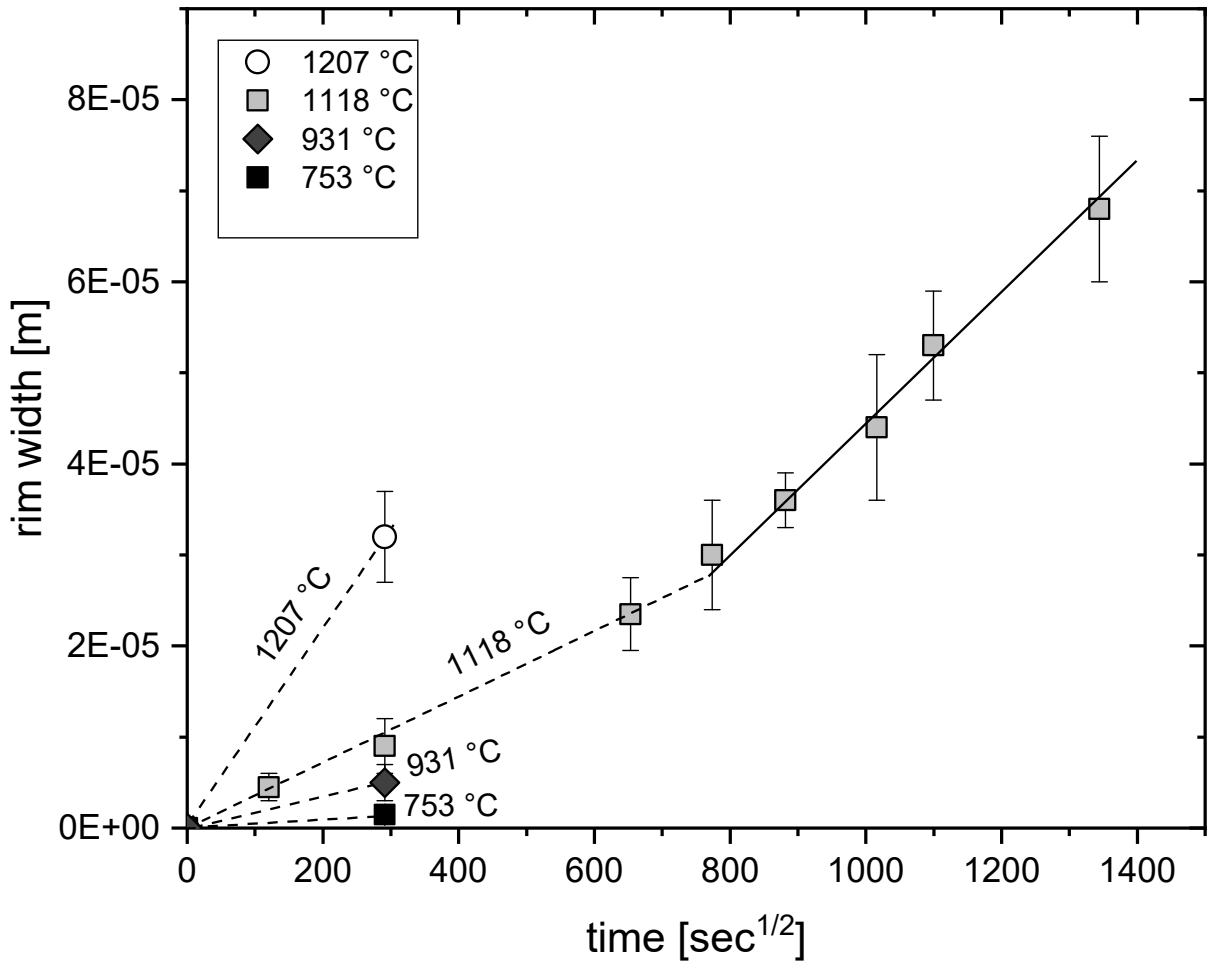

714

715

This is the peer-reviewed, final accepted version for American Mineralogist, published by the Mineralogical Society of America.
The published version is subject to change. Cite as Authors (Year) Title. American Mineralogist, in press.
DOI: https://doi.org/10.2138/am-2021-7588. http://www.minsocam.org/

716 **Figure 9**

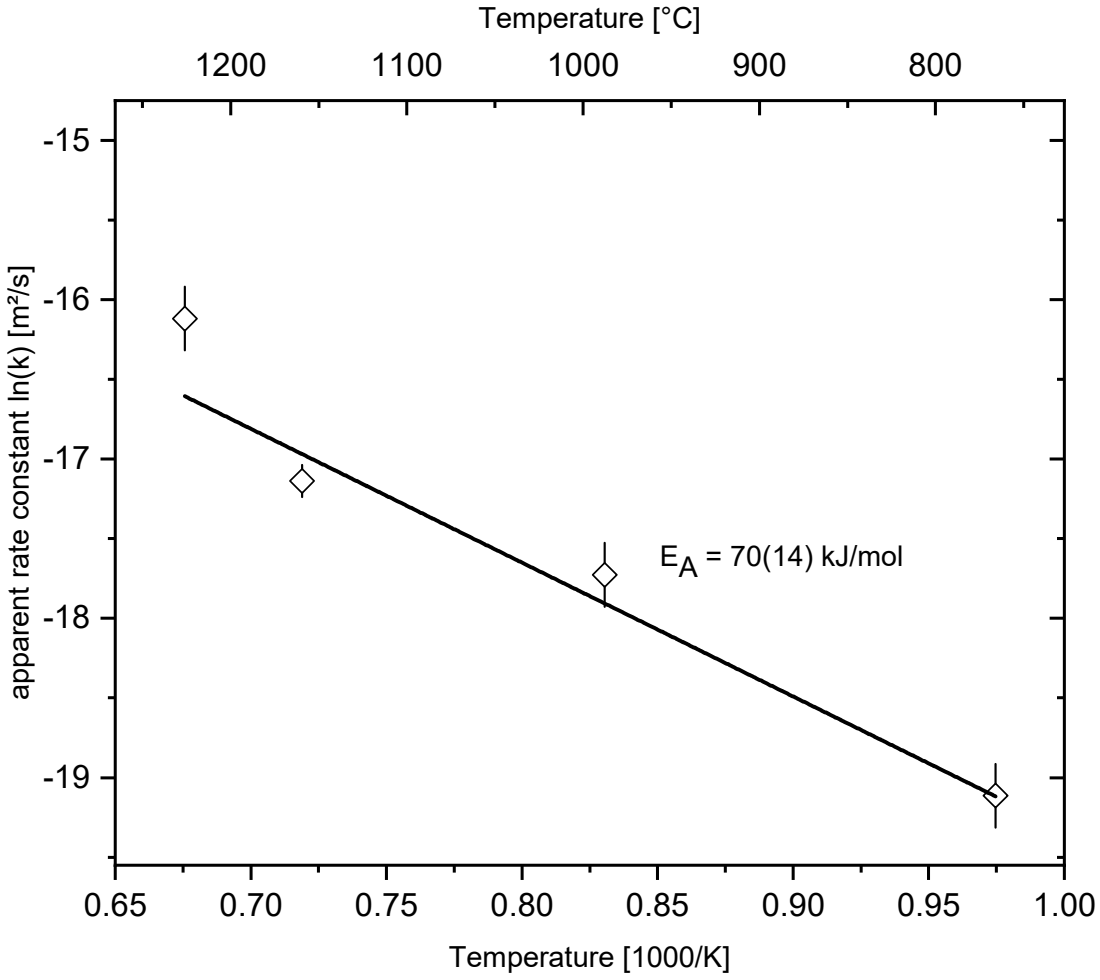

717

718

This is the peer-reviewed, final accepted version for American Mineralogist, published by the Mineralogical Society of America.
The published version is subject to change. Cite as Authors (Year) Title. American Mineralogist, in press.
DOI: https://doi.org/10.2138/am-2021-7588. http://www.minsocam.org/

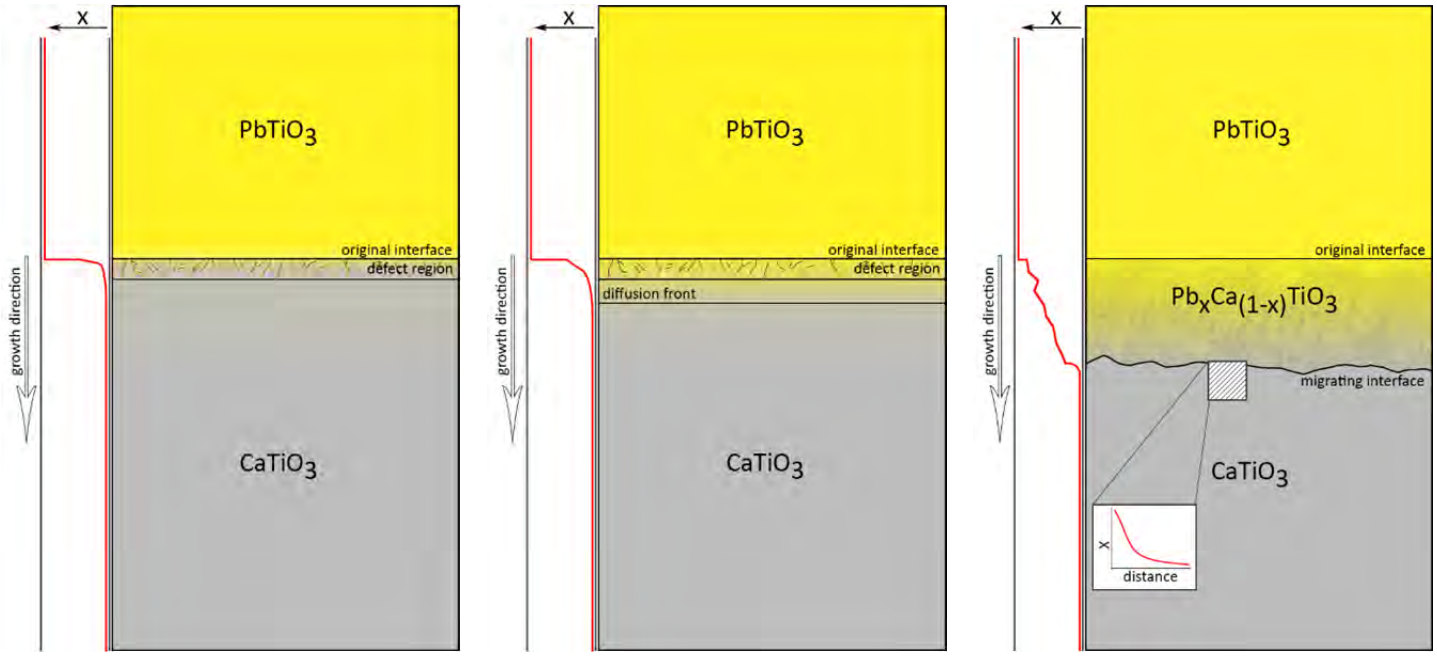

719 **Figure 10**

720

721

This is the peer-reviewed, final accepted version for American Mineralogist, published by the Mineralogical Society of America.
The published version is subject to change. Cite as Authors (Year) Title. American Mineralogist, in press.
DOI: https://doi.org/10.2138/am-2021-7588. http://www.minsocam.org/

722 **Figure 11**

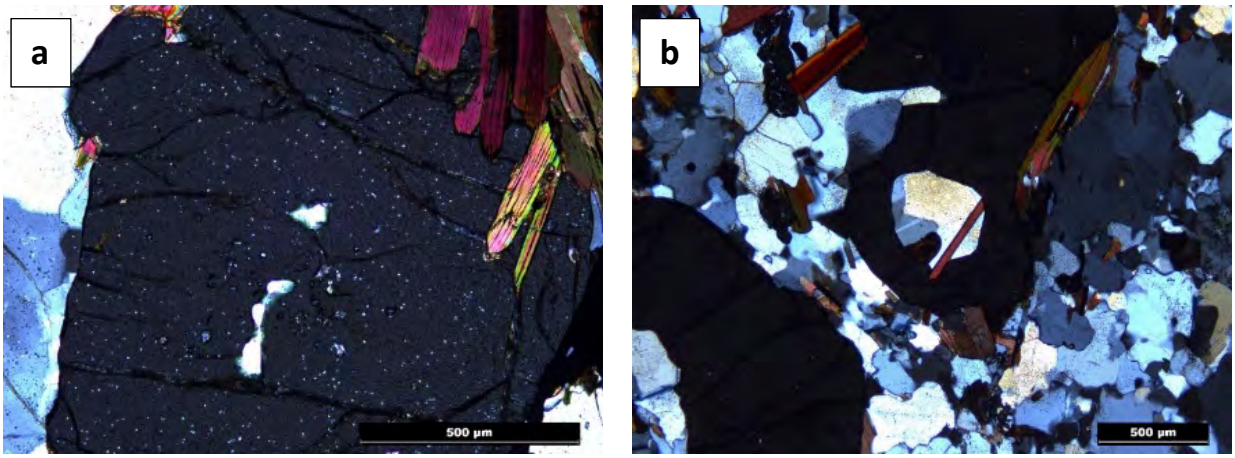

723